Corrosion Science 205 (2022) 110413

Contents lists available at ScienceDirect

Corrosion Science

journal homepage: www.elsevier.com/locate/corsci

High temperature oxidation resistance of physical vapor deposited Hf-Si-$B_{2\pm z}$ thin films

T. Glechner [a,*], A. Bahr [a], R. Hahn [a], T. Wojcik [a], M. Heller [b], A. Kirnbauer [c], J. Ramm [d], S. Kolozsvari [e], P. Felfer [b], H. Riedl [a,c]

[a] Christian Doppler Laboratory for Surface Engineering of High-Performance Components, TU Wien, Austria
[b] Department of Materials Science, Friedrich-Alexander-Universität Erlangen-Nürnberg, DE-91058 Erlangen, Germany
[c] Institute of Materials Science and Technology, TU Wien, A-1060 Wien, Austria
[d] Oerlikon Balzers, Oerlikon Surface Solutions AG, FL-9496 Balzers, Liechtenstein
[e] Plansee Composite Materials GmbH, D-86983 Lechbruck am See, Germany

ARTICLE INFO

Keywords:
Hf-Si-B
Ultra-high temperature
Si diffusion
Oxidation
PVD
TEM
APT

ABSTRACT

Within physical vapor deposited Hf-Si-$B_{2\pm z}$ thin films, selective diffusion-driven oxidation of Si is identified to cause outstanding oxidation resistance at temperatures up to 1500 °C. After 60 h at 1200 °C, the initially 2.47 μm thin $Hf_{0.20}Si_{0.23}B_{0.57}$ thin film exhibits a dense oxide scale of only 1.56 μm. The thermally induced decomposition of metastable Hf-Si-$B_{2\pm z}$ leads not only to the formation of Si precipitates within the remaining thin film (related to a non-homogenous Si distribution after the deposition) but also to pure Si layers on top and bottom of the Hf-Si-$B_{2\pm z}$ coatings next to the excellent adherend SiO_2 based scales.

1. Introduction

Extending the lifetime and operating ranges of highly stressed components used in aviation or energy production is a prerequisite to achieving desired efficiency criteria and guaranteeing a sustainable use of resources. High-temperature processes are the key in various applications, demanding new materials or concepts to enhance their capability withstanding extreme environments – especially oxidative attacks above 1100 °C [1]. Surface modifications are well-established to protect the underlying components. Typically, thermally exposed machine elements (i.e. turbine blades) made of Ni-based super-alloys are protected against oxidation by MCrAlY coating materials [2,3], where an additional thermal barrier coating (TBC) on top even enhances the operation temperatures up to 1200 °C (i.e. yttrium stabilized zirconia [4]). However, to reach even higher temperatures, new coating concepts are needed. Furthermore, new, non-established bulk materials retaining their mechanical properties at even higher temperatures – in detail, ceramic matrix composites (e.g. C/C, C/SiC, and SiC/SiC) – have specific requirements for protective coating materials. In fact, properties such as low thermal expansion coefficients, a strongly retarded oxygen diffusion, or enhanced water vapor stability are essential [5].

In a recent study, physical vapor deposited (PVD) silicon alloyed transition metal (TM) diboride thin films (TM-Si-$B_{2\pm z}$, TM= Ti, Cr, Hf, Ta, W) are suggested as highly durable protective coating materials, sustaining temperatures beyond 1200 °C in oxidative atmospheres [6]. This group of materials combines the outstanding thermal stability and mechanical properties of TM-diborides [7] with the excellent oxide former Si, being a well-established approach in the field of TM-diboride bulk ceramics (addition of SiC or metal silicides) [8–10]. Previous studies also highlighted the potential of silicon alloyed ZrB_2 PVD coatings [11,12]. Furthermore, in various studies sintered HfB_2-SiC based thick coatings (>100 μm) have been proven to provide excellent oxidation protection for C/C composites [13–15]. A temperature-dependent oxide scale formation is predominant for Si alloyed bulk TM-diborides and coatings, respectively [6,16]. Below ~1050 °C, a layered scale consists of a TM-oxide and an amorphous B-rich scale on top, similar to binary TM-diborides [17]. In contrast, above ~1050 °C B_2O_3 evaporation becomes significant, and a highly protective glassy like Si-rich oxide scale is formed [6,16]. However, in contrast to bulk ceramics the oxidation rates are reported to be three orders of magnitude lower for PVD coatings at 1100 °C [6,16]. HfB_2 as the binary system of a Hf-Si-$B_{2\pm z}$ coating stands out due to its high

* Corresponding author.
E-mail address: thomas.glechner@tuwien.ac.at (T. Glechner).

https://doi.org/10.1016/j.corsci.2022.110413
Received 3 February 2022; Received in revised form 28 April 2022; Accepted 27 May 2022
Available online 2 June 2022
0010-938X/© 2022 The Authors. Published by Elsevier Ltd. This is an open access article under the CC BY license (http://creativecommons.org/licenses/by/4.0/).

thermal stability (highest melting point of all diborides [18]), high hardness [19], and excellent oxidation resistance [19] – compared to other binary transition metal diboride coating materials [16,20–22]. The formed TM-oxide, HfO_2, also exhibits the highest thermal and chemical stability [23]. Nevertheless, to increase the oxidation resistance, Si alloying is an auspicious approach for HfB_2 based PVD coatings. In contrast to bulk ceramics or thick coatings synthesized from powders where Si is present as a separate phase (e.g. SiC, $MoSi_2$, $TaSi_2$), physical vapor deposited TM-Si-$B_{2\pm z}$ thin films appear single phased in the XRD spectra, hence being depended on the Si diffusion behavior. Due to the limited kinetics during physical vapor deposition – extremely high cooling rates and non-equilibrium conditions – metastable phases such as α-structured TM-Si-$B_{2\pm z}$ are accessible (α-AlB_2 prototype, space group 191, *P6/mmm*). Typically, TM-Si-$B_{2\pm z}$ thin films either prevail in the hexagonal diboride structure or prefer an amorphous state [6,11,24]. The Si distribution in the as deposited state plays a crucial role in the oxidation resistance. The formation of Si rich oxide scales is preferred by fast track diffusion processes, e.g. along grain or column boundaries [25]. According to the ternary Hf-Si-B phase diagram at 1300 °C [26], HfB_2 exhibits a very low solubility for Si, hence a phase separation after thermal impacts is expected.

Therefore in the present study, we investigate in detail the high-temperature oxidation behavior of Hf-Si-$B_{2\pm z}$ PVD thin films with varying Si concentrations and try to describe the cause for the specific low oxide growth rates. A particular focus lies on the long-term (up to 60 h) oxidation behavior of these coating materials at 1200 °C and beyond. Furthermore, the occurring Si diffusion in relation to the singled phased structure in the as deposited state, as well as the phase separation mechanisms, are investigated.

2. Methods

All thin films were deposited in an in-house built magnetron sputtering system [27] using a circular 3 in. HfB_2 target (Plansee Composite Materials GmbH), operated in DC mode with a constant current of 0.5 A. Argon was used as working gas, 0.56 Pa, also described a previous study [6]. Additional Si was added to the thin films by evenly placing single crystalline Si plates (7×7× 0.38 mm) on the target racetrack. By varying the number of pieces (5–8), the Si content is adjusted within the thin films. The thin films were deposited on sapphire (10×10×0.53 mm^3), and single crystalline SiC (4 h, 20×7x 0.38 mm^3) substrates. The target to substrate distance was set to 90 mm. The substrates were cleaned with acetone and ethanol, and furthermore plasma cleaned in the sputter system before the deposition. For all thin films, a substrate temperature of 550 °C as well as a bias potential of − 40 V were used.

X-ray photoelectron spectroscopy (XPS) measurements were conducted in a custom-built SPECS XPS-spectrometer equipped with a monochromatic Al-K_α (1486.6 eV) X-ray source (μFocus 350, spot size: 450 μm, power: 70 W) and a hemispherical WAL-150 analyzer (acceptance angle 60°). Before recording the overview and detail spectra, the sample was sputter cleaned for 120 s on a 2 × 2 mm^2 area using 3 kV Ar-ions at a pressure of $2\bullet10^{-5}$ Pa (angle between Ar beam and sample surface normal: 45°). The detail spectra of Hf, Si, and B were recorded with a pass-energy of 30 eV, and an energy resolution 0.1 eV. The recorded spectra were analyzed using transmission corrections (as per manufacturer's specifications), Shirley-backgrounds [28], and sensitivity parameters after Scofield [29]. Within CASA XPS, charge corrections, by setting the binding energy value of adventitious carbon from minor surface contamination to 284.8 eV, according to ISO 15472:2010, were done. Deconvolution of XPS signals was carried out using symmetric Gaussian- Lorentzian peaks (GL(30)) and Levenberg-Marquardt least-square peak fitting.

For Atom Probe Tomography (APT) analysis, the coated Si wafer samples were precut with a microPREP™ Laser cutter. An outer box cut was carried out, cutting the entire sample away just leaving rectangular pillars behind. A laser power of 0.5 W and an area dose of 5 pulses/μm^2 was used. The remaining pillars were cut with the laser cutter into smaller circular pillars with an outer diameter of 20 μm with a laser energy of 0.1 W and an area dose of 15 pulses/μm^2. Afterwards, the final pillar milling and sharpening of the tip was performed with a focused ion beam microscope ZEISS Crossbeam 540. Adjacent APT analysis was carried out on a CAMECA LEAP 4000X HR in pulsed laser mode with a pulse energy of 50 pJ. The instrument is equipped with a 355 nm UV laser and a reflection lens. This enables a detection efficiency of ~37%. The specimen temperature was at 44 K, the target evaporation rate was 1% and pulse rate was set to 200 kHz. Data analysis was performed with a Matlab Toolbox [30] for analyzing atom probe data.

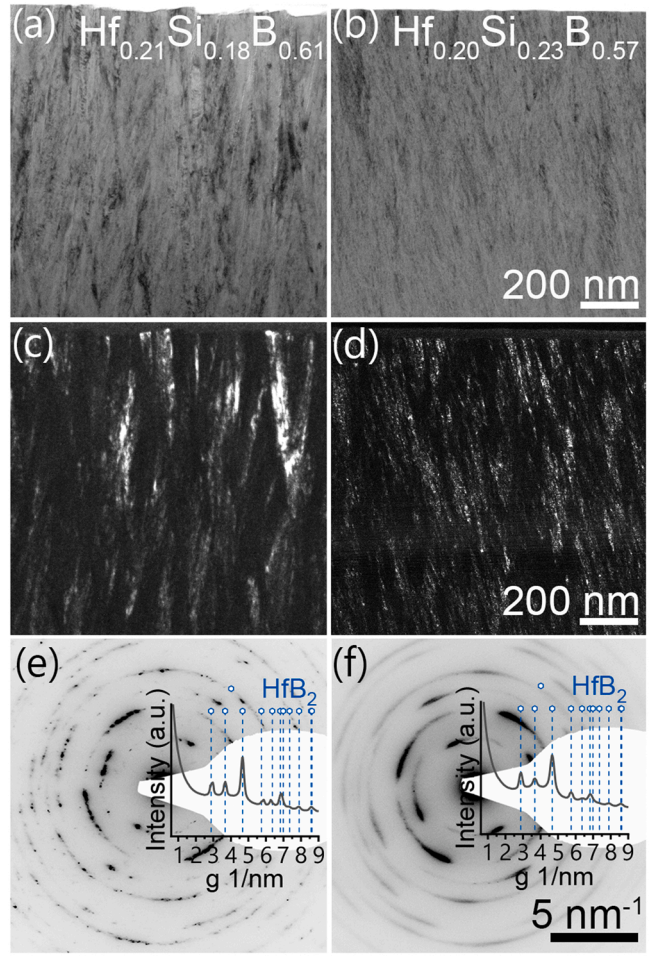

Fig. 1. TEM bright field (a, b) and dark field (c, d) image of $Hf_{0.21}Si_{0.18}B_{0.61}$ and $Hf_{0.20}Si_{0.23}B_{0.57}$ in the as deposited state. (e,f) Corresponding selected area electron diffraction (SAED) images. The intensity integrations plotted as an overlay in (e,f) was done using CrysTBox [45,46].

Isothermal oxidation was performed in a conventional box furnace in ambient air. The thin films on sapphire substrate were put into the preheated furnace, whereas thin films on SiC substrates stayed in the furnace since room temperature. To reduce thermal stresses during heating, a heating rate of ~25 K/min was used. After the desired time, the thin films on sapphire substrates were directly put out of the furnace and cooled down in ambient air to room temperature. For the thin films on SiC substrate the furnace was cooled down to 900 °C with ~100 K/min and subsequently cooled down passively in ambient air.

To determine the crystal structure X-ray diffraction (XRD) analysis was done in Bragg Brentano configuration, using a Panalytical XPert Pro MPD diffractometer equipped with a Cu-K_α radiation source (wavelength λ = 1.5418 Å). Cross sections of the oxidized samples were prepared using a Thermo Scientific Scios 2 (FIB-SEM Dual beam system) equipped with Ga^+ ion source. Cross-section windows of 12 × 7 μm

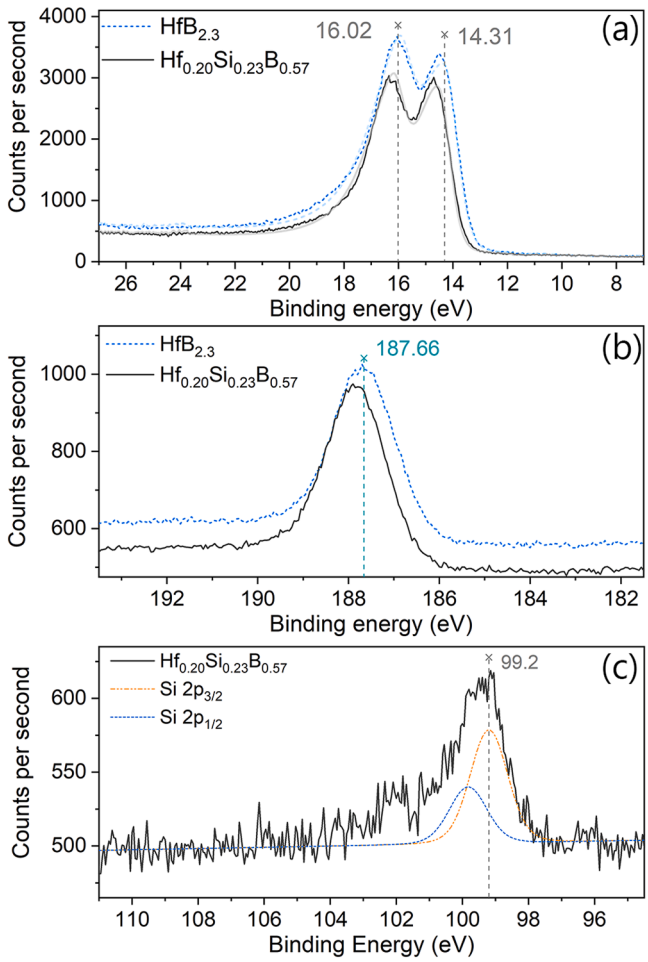

Fig. 2. Hf 4f (a), B 1s (b) and Si 2p peak (c) determined for $HfB_{2.3}$ and $Hf_{0.20}Si_{0.23}B_{0.57}$ applying XPS.

were milled using ion beam current of 7–15 nA for rough milling and 1 nA for fine milling. The acceleration voltage was set to 30 kV. The cross-section images were taken using the same system in SEM mode at an acceleration voltage of 5 kV. Furthermore, the FIB system Thermo Scientific Scios 2 was used to prepare cross-sectional lamellas of the thin films in the as deposited and oxidized state for further investigation in a transmission electron microscopy (TEM). The TEM studies were performed on a FEI TECNAI F20, equipped with a field emission gun and operated at an accelerating voltage of 200 kV. Bright field (BF) dark field (DF) imaging and selected area electron diffraction (SAED) reveals the microstructure, crystal structures and texture, whereas high angle annular dark field (HAADF, mass contrast) images and energy dispersive x-ray spectroscopy (EDX) line scans in scanning TEM (STEM) mode provide information about the chemical composition.

3. Results and discussion

$Hf_{0.21}Si_{0.18}B_{0.61}$, $Hf_{0.20}Si_{0.23}B_{0.57}$, and $Hf_{0.20}Si_{0.25}B_{0.55}$ thin films (subscript denote chemical composition in at%) were grown in pure Ar atmosphere (chemical analysis done with ICP-OES is described in Ref. [6]) exhibiting coating thicknesses of 2.40, 2.47, and 2.60 μm, respectively. For these compositions, the formation of the desired highly protective Si-rich scale is reported in a previous study by the authors, which contains a broader screening process of different Si alloyed transition metal diborides [6]. All three thin films appear single phase structured in XRD analysis (see also Fig. A1 in the Appendix), displaying only peaks corresponding to the α-HfB_2 structure, with no indications for any silicide-based phases. To gain a more detailed insight on the phase formation during synthesis and especially to the influence of Si on α-structured HfB_2 thin films TEM analysis has been conducted. Here we would like to mention, that we focused the analysis with high resolution techniques on $Hf_{0.20}Si_{0.23}B_{0.57}$, which was found to have the lowest Si content required for long term stability in an oxidative environment.

In Fig. 1 the morphology of $Hf_{0.21}Si_{0.18}B_{0.61}$ and $Hf_{0.20}Si_{0.23}B_{0.57}$ is compared. For both coatings dense and V-shaped columnar structures are clearly visible in bright and dark field imaging mode – see Fig. 1a–d. The mean column diameter, estimated using the dark field images, decreases from about 31–12 nm with increasing Si content. The V-shaped columnar structure is based on so-called competitive growth during physical vapor deposition [31], whereas Si is known to be a grain boundary active element during film growth leading forcing crystals to smaller column diameters [32]. This is further confirmed by SAED analysis, where still single spots are visible for the low Si containing $Hf_{0.21}Si_{0.18}B_{0.61}$ (see Fig. 1e), whereas for $Hf_{0.20}Si_{0.23}B_{0.57}$ the spots are circularly blurred (see Fig. 1f). Selected area electron diffraction shows also no indications of a separate silicon-based phase in the as deposited state. To get further insights about the constitution of Si within the coatings, the bonding nature was investigated using XPS, comparing $Hf_{0.20}Si_{0.23}B_{0.57}$ with the binary $HfB_{2.3}$. Details on the deposition and further properties of the $HfB_{2.3}$ coating can be found in Ref. [19]. Fig. 2 summarizes the Hf 4 f (see a) and B 1 s (see b) peaks for $HfB_{2.3}$ (dashed blue line) and $Hf_{0.20}Si_{0.23}B_{0.57}$ (solid black line), respectively, and additionally shows the Si 2p peak (c) for the Si containing $Hf_{0.20}Si_{0.23}B_{0.57}$ coating. In Fig. 2a, the indicated peak positions of Hf 4 $f_{7/2}$ (16.02 eV) and Hf 4 $f_{5/2}$ (14.31 eV) belong to the binary $HfB_{2.3}$ coating, where both Hf 4 f peaks are shifted by about 0.2 eV to higher binding energies with the addition of Si. This shift can be either caused by the different B/Hf ratio of the two coatings, or due to the additional Si surrounding Hf and B atoms. Furthermore, the position of the B 1 s peak is also displaced by about 0.2 eV for the $Hf_{0.20}Si_{0.23}B_{0.57}$ coating with respect to $HfB_{2.3}$, but in principal agrees well with the binary HfB_2 state (187.5 eV [33]) – see Fig. 2b. For the Si alloyed $Hf_{0.20}Si_{0.23}B_{0.57}$ coating the position of the Si $2p_{3/2}$ peak is very close to the one of pure silicon, 99.4 eV. In Ref. [34] for $HfSi_2$ a Hf 4 $f_{7/2}$ peak position of 14.65 eV is

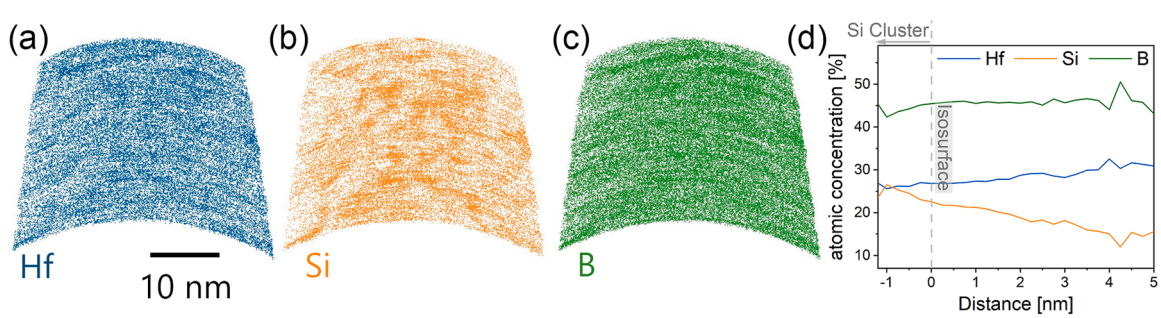

Fig. 3. 5 nm slice of the APT tip for $Hf_{0.20}Si_{0.23}B_{0.57}$, where the individual atomic species are plotted in (a), (b) and (c). (d) shows the chemical environment of a Si cluster obtained from a Si isosurface analysis. Distance below 0 represents the area within the Si isosurface and hence Si cluster.

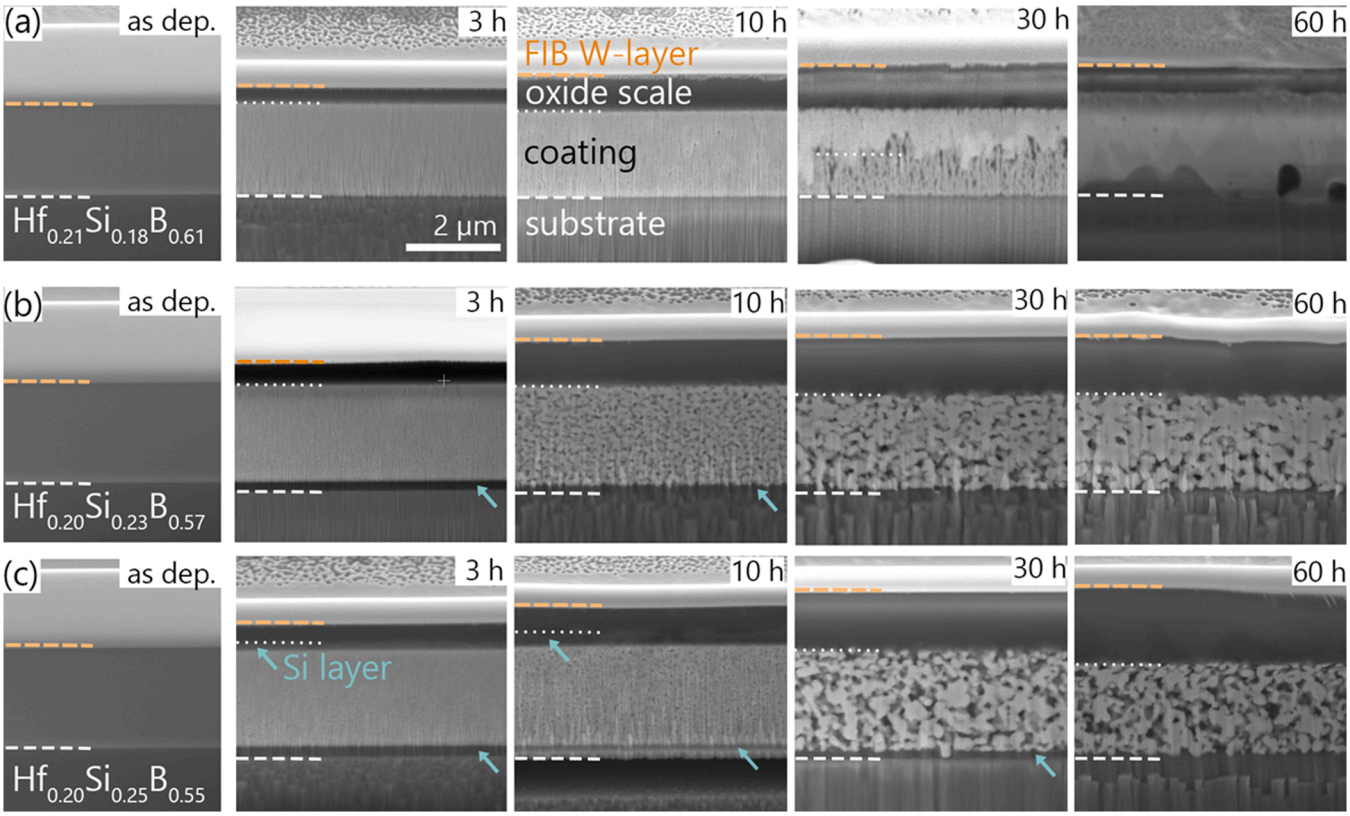

Fig. 4. FIB cross sections of $Hf_{0.21}Si_{0.18}B_{0.61}$ (a), $Hf_{0.20}Si_{0.23}B_{0.57}$ (b) and $Hf_{0.20}Si_{0.25}B_{0.55}$ (c) on sapphire substrate oxidized at 1200 °C for 3, 10, 30 and 60 h. Dashed and dotted lines indicate the substrate/coating and coating/oxide scale interface respectively. The bright appearing layer on top is a tungsten layer deposited in the FIB system and the interface between this layer and the oxide scale is indicated by orange dashed lines. Cyan arrows indicate Si layers formed during oxidation.

reported as well as a Si $2p_{3/2}$ peak position that is indistinguishable from pure Si. Furthermore, in Ref. [35] peak positions for B 1 s of 188.4 eV and Si 2p of 102.8 eV are reported for SiB_4. Comparing the peak positions of this study to compounds where Si is on the one hand bonded to Hf ($HfSi_2$) and on the other hand to B (SiB_4), no clear conclusion about the bonding stated in Hf-Si-$B_{2\pm z}$ can be drawn. The fact that the peak positions for both Hf 4 f and B 1 s are shifted by the same amount in the Si containing coating rather suggests a variation by the changed B/Hf ratio (2.3 – 2.85) than due to Hf-Si or B-Si bonds.

To further determine the chemical distribution of Si within Hf-Si-$B_{2\pm z}$ thin films APT analysis have been conducted for $Hf_{0.20}Si_{0.23}B_{0.57}$ in the as deposited state. A 5 nm slice of the measured tip is shown in Fig. 3a–c, with the different elements Hf, Si, and B, respectively. One can clearly see that Si is not evenly distributed within the film, but forms small clusters – see more intense regions in Fig. 3b. To determine, if there is a further Hf or B accumulation at these silicon enriched clusters, Si isosurfaces (15 at% Si) have been determined. The mean elemental distribution from the midst of the cluster (distance <0) out of the isosurfaces (distance > 0) is plotted in Fig. 3d. Through this approach we can highlight that, Si clusters are only formed in boron and hafnium depleted zones - equal decrease inside the isosurface and hence Si cluster. This uneven distribution of Si in the as deposited coating, is furthermore in good agreement with the limited solubility of Si in HfB_2 as suggested by the ternary phase diagram [26]. However, a direct correlation between the morphology – in detail grain boundaries – or the crystal lattice with respect to Si sides could not be verified. The observed decreasing grain size might be an indication, that Si segregates at the grain boundaries as it is observed for Ti-Si-N, where a SiN_x tissue phase at the grain boundaries is reported [36].

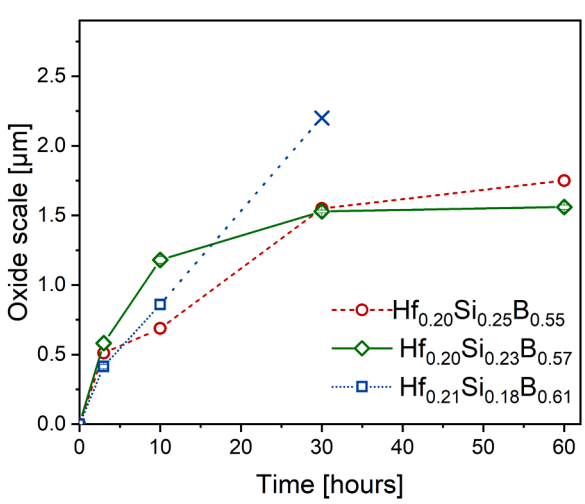

Fig. 5. Oxide scale thicknesses in relation to oxidation time at 1200 °C for all thin films investigated.

To determine their oxidation kinetics at 1200 °C, we oxidized the 3 different samples with increasing Si content (18, 23, and 25 at%) deposited on sapphire substrates in ambient air for 3, 10, 30, and 60 h, respectively. A detailed analysis of the formed oxide scales was done via FIB cuts, where a thin tungsten layer was deposited on the surface (bright appearing) and a window was milled into the thin films afterwards, as indicated in Fig. 4a after 10 h. For the three Hf-Si-$B_{2\pm z}$ compositions, the unoxidized coatings are shown on the left-hand side, appearing highly dense also in the FIB cuts. After 3 h at 1200 °C the thin films with the lowest Si content of 18 at% exhibits the least oxide scale thickness of 415 ± 15 nm, which is about 180 nm less than for $Hf_{0.20}Si_{0.23}B_{0.57}$ (580 ± 20 nm). The oxide scale thickness of

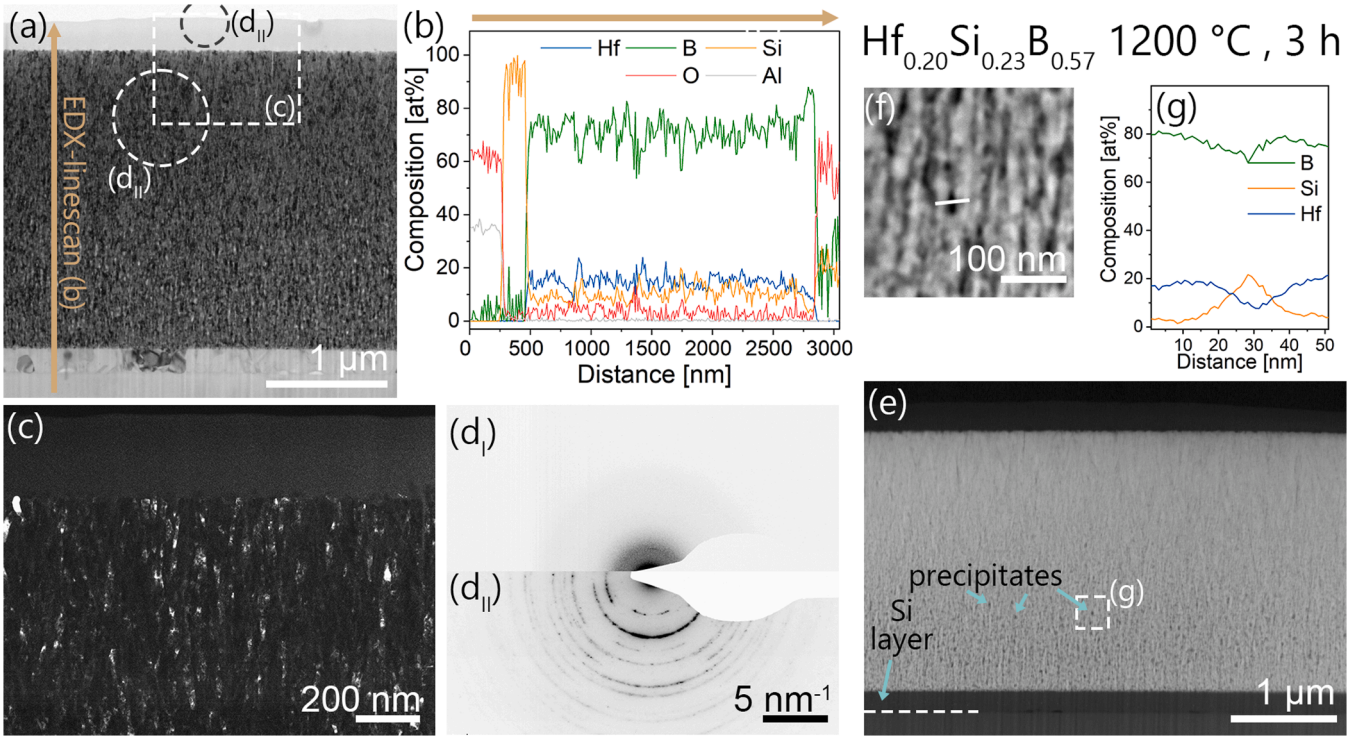

Fig. 6. TEM analysis of $Hf_{0.20}Si_{0.23}B_{0.57}$ on sapphire substrate, oxidized for 3 h at 1200 °C. (a) Bright field (BF) image of the whole oxidized coating with corresponding EDX line scan (b). The dark field (DF) image shows the oxide scale and remaining coating (c) and the two selected area electron diffraction (SAED) images further depict the amorphous and crystalline appearance of the oxide scale (d_I) and remaining coating (d_{II}) respectively. (e) High angle annular dark field (HAADF) image of the whole oxidized coating and the coating/substrate interface indicated by a white dashed line. Cyan arrows indicate the formed Si layer and Si precipitates. (f) EDX line scan over a dark appearing region shown in (g) and (e).

$Hf_{0.20}Si_{0.25}B_{0.55}$ is with 510 ± 40 nm just in between. Furthermore, a thin Si interlayer forms at the coating/substrate interface for $Hf_{0.20}Si_{0.23}B_{0.57}$ and $Hf_{0.20}Si_{0.25}B_{0.55}$, after 3 h see Fig. 4b and c (indicated by cyan arrows). In addition, for the highest Si content of $Hf_{0.20}Si_{0.25}B_{0.55}$ also a Si enriched zone at the unaffected coating to scale interface was identified – see Fig. 4c after 30 h. After 10 h the two thin films with the higher Si content exhibit first indications of recrystallization processes, being more intensified after 30 h, see also the formation of small voids within the unoxidized region. On the other hand, $Hf_{0.21}Si_{0.18}B_{0.61}$ forms monoclinic (m) HfO_2 after 30 h (verified by EDX and XRD), accompanied by the spallation of most of the residual coating (maybe related to internal stresses based on different expansion coefficients). After 60 h the coating is completely oxidized. The FIB cuts in Fig. 4a 30 and 60 h show parts of the remaining coating on the substrate. However, the two coatings with higher Si content were still intact after 60 h, but exhibiting a recrystallized microstructure with some voids and a dense oxide scale on top featuring no signs of spallation. This void formation might be caused by the diffusion of Si out of the coating to the oxide scale and hence leaving an open space.

To illustrate the oxide growth kinetics, the obtained scale thicknesses (Δx) in relation to the oxidation duration are summarized in Fig. 5. At the initial state of oxidation up to 3 h all three thin films perform relatively similar. However, between 3 and 10 h the oxide growth rate of $Hf_{0.20}Si_{0.25}B_{0.55}$ is decelerated due to the above-mentioned Si layer formed at the scale/coating interface. Sometime between 10 and 30 h this Si layer is consumed and therefore the scale thickness exhibits a jump and approaches the oxide thickness of $Hf_{0.20}Si_{0.23}B_{0.57}$ (see red circle at 30 h in Fig. 5). On the other hand, $Hf_{0.21}Si_{0.18}B_{0.61}$ almost linearly increases the oxide thickness and fails due to spallation after 10 h at 1200 °C, whereas the oxide growth rate for $Hf_{0.20}Si_{0.23}B_{0.57}$ is strongly decreased after 10 h. To describe the growth kinetics of $Hf_{0.20}Si_{0.23}B_{0.57}$ the known parabolic rate law does not fit since the observed scale thickness increase is significantly smaller for longer times. The scale thickness-time dependency for $Hf_{0.20}Si_{0.23}B_{0.57}$ is best described using the so called cubic rate law (semi-empirical rate description in relation to Ref. [37]), Eq. (1), which is commonly used to model the oxidation kinetics of MAX phases as reported in more detail Ref. [38].

$$x^3 = k_c\, t \tag{1}$$

With x being the oxide scale thickness, t the time and k_c the cubic rate constant ($k_c = 1.8{\cdot}10^{-23}\ m^3s^{-1}$ for $Hf_{0.20}Si_{0.23}B_{0.57}$). However, the fact that the observed growth kinetics for $Hf_{0.20}Si_{0.25}B_{0.55}$ and also $Hf_{0.20}Si_{0.23}B_{0.57}$ are not perfectly following the mentioned cubic rate law, points towards a changing constitution of the oxide scale with time e.g. through the formation of cristobalite as shown later on in the manuscript. Nevertheless, the obtained growth kinetics clearly suggest that Hf-Si-$B_{2\pm z}$ coatings are suitable for long time oxidation protection, above a certain Si content. After 60 h the oxide scale thickness of $Hf_{0.20}Si_{0.23}B_{0.57}$ and $Hf_{0.20}Si_{0.25}B_{0.55}$ is 1.56 and 1.81 µm respectively. The thickness of the remaining void containing coatings is 2.34 and 2.30 µm, respectively. Hence, the as deposited coating thickness was decreased by only 130 nm for $Hf_{0.20}Si_{0.23}B_{0.57}$, but of course the density decreased too, due to the void formation. Furthermore, the obtained oxide thicknesses at 1200 °C is lower compared to the alumina based oxide scales of MAX (Ti_2AlC [39]) or MAB phases (MoAlB [38,40]) and slightly above the oxide scale thickness of pure Si [41]. This further reflects the fact that above 1100 °C silica forming materials exhibit the lowest scale growth rates [23]. A comparison with two commonly used protective physical vapor deposited (PVD) coating systems, Ti-Al-N and Ti-Si-N, shows that long term stability is guaranteed for these coatings only for much lower temperatures, being in the range of 800–950 °C [42,43]. In contrast to the diboride based TM-Si-$B_{2\pm z}$ coatings, Ti-Si-N coatings do not form a separate silicon oxide layer, but an amorphous Si-O-N phase is formed between the TiO_2 grains [43].

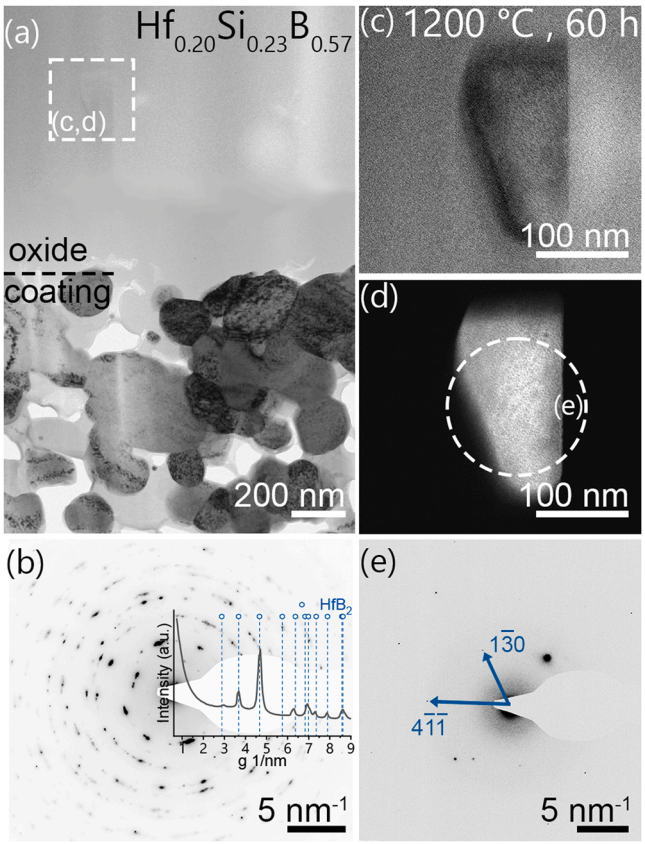

Fig. 7. $Hf_{0.20}Si_{0.23}B_{0.57}$ oxidized at 1200 °C for 60 h. (a) BF image at the interface between the remaining recrystallized coating and amorphous oxide scale. BF image consists of two stitched images. (b) SAED image of the remaining coating including an intensity integration, done using CrysTBox [45, 46], with HfB_2 reference positions. In (c) and (d) a magnified BF and DF image of a crystalline region in the otherwise amorphous oxide scale is shown. In the SAED image (e) blue arrows indicate the cristobalite SiO_2 structure (SG 92) in zone axis [1,3,11].

To gain a detailed understanding of the scale formation of these Hf-Si-$B_{2\pm z}$ thin films, HR-TEM analysis was performed for $Hf_{0.20}Si_{0.23}B_{0.57}$ after 3 and 60 h, respectively. TEM analysis of $Hf_{0.21}Si_{0.18}B_{0.61}$ after 3 h can be found in Ref. [6]. Fig. 6 gives a closer look into the oxide scale and the remaining coating after 3 h at 1200 °C oxidation in ambient air. The BF image (a) and corresponding EDX Line scan (b) indicate an amorphous (see SAED analysis in Fig. 6d_I) oxide on top of the unaffected coating containing no Hf. Beneath this oxide the unaffected, crystalline coating (see also the corresponding SAED in Fig. 6d_{II}) as well as a uniform 200 nm thick Si layer at the coating substrate interface is visible. This Si enriched layer is not present in the as deposited state and, hence was formed through Si diffusion out of the thin film during oxidation. Furthermore, due to the low accuracy of EDX in quantifying light elements, the boron content is overestimated in the coating as well as in the oxide scale, see green line in Fig. 6b. Additional electron energy loss spectrometry (EELS) analysis of just the oxide scale suggests, that the boron content within the scale is only in the range of a few atomic percent (≤3 at%), as also shown for $Hf_{0.21}Si_{0.18}B_{0.61}$ in Ref. [6]. Comparing the SAED and dark field images of $Hf_{0.20}Si_{0.23}B_{0.57}$ in the as deposited state (Fig. 1d) and after 3 h at 1200 °C (Fig. 6c,d) one can see the initiated phase formation and recrystallization processes. The mean width of the columnar grains determined from DF images increased from ~12 nm in the as deposited state to ~17 nm. Furthermore, small precipitates form in the remaining coating, above the Si enriched zone at the substrate to coating interface, appearing dark in the HAADF image (Fig. 6e) and indicated by cyan arrows. Based on a more detailed EDX analysis (see Fig. 6f and g), these precipitates are clearly identified as Si precipitates. Along with the formed Si interlayer, this points towards a strong driving force of Si to diffuse out of the α-structured HfB_2 upon annealing. The ternary phase diagram of the Hf-B-Si system at 1300 °C [26] suggests a very low solubility of Si in the HfB_2 structure (<1 at%) and a two phase field of HfB_2 and Si (SG 227, diamond prototype) with increasing Si content at a constant B/Hf ratio of 2. This is a strong indication for the observed transformation of the metastable state, where a high amount of silicon is dissolved in the HfB_2 structure, into the thermodynamic stable states where Si and HfB_2 are present as separate phases. Interestingly no phase separations are observed for $Hf_{0.21}Si_{0.18}B_{0.61}$ [6] suggesting that there is a minimum Si content for forming crystalline Si precipitates.

After 60 h at 1200 °C in ambient air the remaining $Hf_{0.20}Si_{0.23}B_{0.57}$ thin film further recrystallizes exhibiting large globular grains and small voids, see Fig. 7a. The SAED analysis (Fig. 7b) further confirms the single phase α-HfB_2 structure of the remaining crystalline grains. The oxide scale on top is densely covering the entire surface, but containing small crystalline regions embedded in an amorphous matrix. Such a grain is depicted in more detail in Fig. 7c-d, whereby the dark field image (d) clearly shows the crystalline character within the amorphous oxide scale matrix. A subsequent SAED analysis suggests the cristobalite SiO_2 structure (see Fig. 7e). Interestingly, no obvious HfO_2 is formed even after this long time period and hence the oxide scale is still preferably formed by Si that diffuses out of the coating. Calculating the change in Gibbs' free energy (ΔG_r^o) of reaction (2) and (3) using the FactSage software package (version 8.1) resulted in $\Delta G_r^o = -591$ and -649 kJ/Mol O_2, respectively (at ambient pressure and 1200 °C).

$$HfB_2 \quad (s) + \quad \frac{5}{2} \quad O_2(g) \rightarrow HfO_2 \quad (s) + \quad B_2O_3(l) \tag{2}$$

$$Si \quad (s) + O_2(g) \rightarrow SiO_2 \quad (s) \tag{3}$$

Hence, reaction (3) is thermodynamically favored. Therefore, if the supply of Si at the oxide/coating interface is guaranteed only SiO_2 will form. The supply is apparently driven by Si diffusion, which is further enhanced by the strong phase separation of Si and HfB_2. Here we want to mention that also for the ZrB_2/SiC system the oxidation of SiC is thermodynamically more preferred, but the difference in ΔG_r^o is much smaller [44]. At lower temperatures, the kinetics to oxidize ZrB_2 are higher compared to SiC and hence B_2O_3 and ZrO_2 are reported to form below ~1200 °C [44]. This matches also the observations for PVD TM-Si-$B_{2\pm z}$ thin films in our previous study [6] and hence suggests that the strong Si diffusion and phase separation requires a certain temperature to take over the HfB_2 oxidation route. This selective, diffusion driven oxidation of Si seems to be the key factor for the outstanding oxidation resistance of Hf-Si-$B_{2\pm z}$ thin films.

To further understand the Si diffusion within Hf-Si-$B_{2\pm z}$ thin films and the formation of Si rich phases, we oxidized all thin films on a Si containing substrate material, namely single crystalline SiC. As stated in the introduction the challenge here is the small thermal expansion coefficient of SiC. Hence, the coatings on SiC substrate were put into the furnace at room temperature and heated up to the desired temperature in ambient air at a heating rate of about 25 K/min. After the desired isothermal oxidation, the samples cooled down to 900 °C at a cooling rate of ~100 K/min and then put out of the furnace.

Fig. 8a depicts a cross sectional overview of the $Hf_{0.20}Si_{0.23}B_{0.57}$ coating (deposited on SiC) oxidized at 1200 °C for 3 h. The formed oxide scale on top is composed out of two different layers. In detail, on top a very small globular HfO_2 grains can be identified, followed by an amorphous Si-rich oxide beneath see Fig. 8b. The very thin HfO_2 scale origins from the heating up step. As reported in more detail in Ref. [6] and mentioned in the previous paragraph also for ZrB_2/SiC bulk ceramics, Hf-Si-$B_{2\pm z}$ coatings exhibit a temperature dependent oxide scale formation. Below ~1100 °C the scale consists of two layers – crystalline HfO_2 and an amorphous boron rich oxide on top – whereas above the

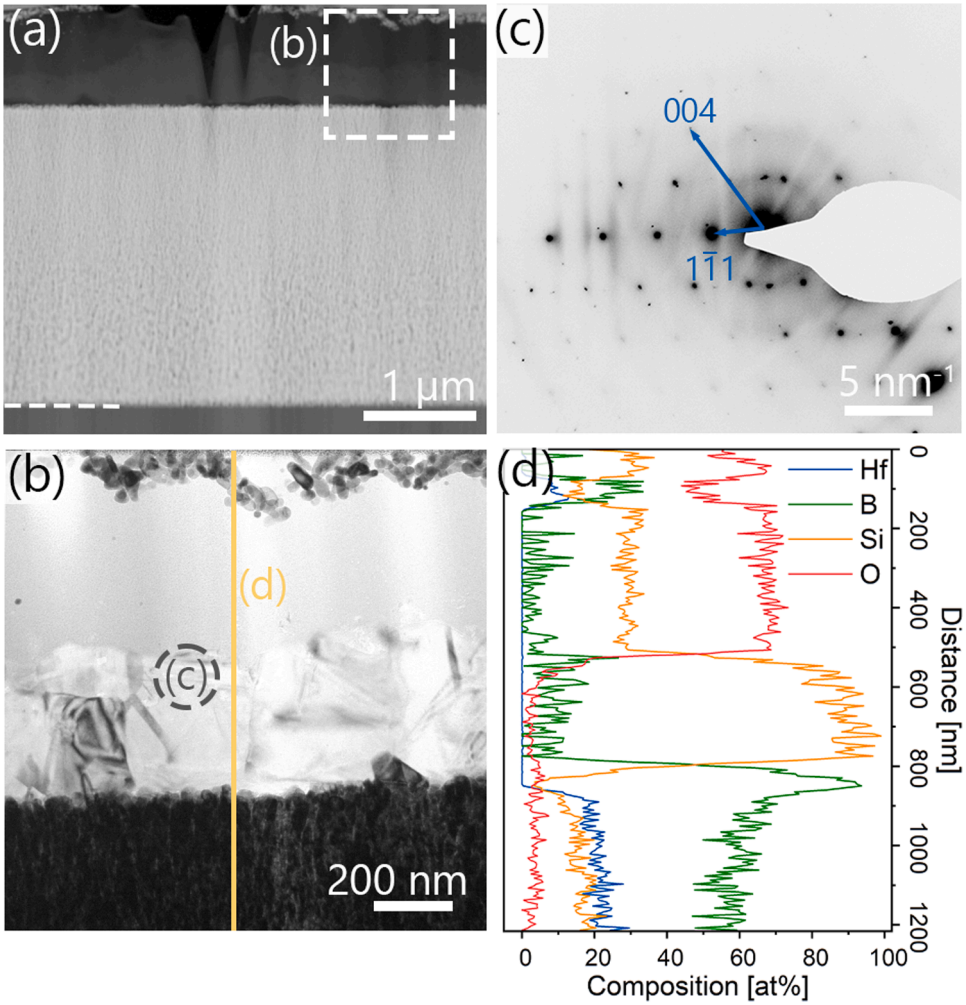

Fig. 8. TEM analysis of $Hf_{0.20}Si_{0.23}B_{0.57}$ deposited on a single crystalline SiC substrate and subsequently oxidized for 3 h at 1200 °C. (a) HAADF overview image of the whole oxidized coating including the substrate/coating interface (indicated by a dashed line). (b) BF image and (d) corresponding EDX line scan of the formed layers above the remaining $Hf_{0.20}Si_{0.23}B_{0.57}$ coating (dark appearing). SEAD image (c) was acquired at zone axis (ZA) = [110] from the dashed circular region in (b).

formation of just an amorphous Si rich oxide is preferred. Hence, during heating up the HfO_2 grains form between ~700 and 1100 °C, above the Si rich oxide is preferred. Below the layered oxide scale, a 390 ± 100 nm silicon layer (see also the EDX line scan in Fig. 8d) is formed exhibiting a cubic diamond structure (SG 227) – confirmed by the SAED image in Fig. 8c. Hence, in contrast to the $Hf_{0.20}Si_{0.23}B_{0.57}$ coating oxidized on sapphire substrate, where a Si interlayer has formed at the substrate coating interface, the SiC substrate promotes only outward diffusion of access Si towards the surface. The oxide scale exhibits a thickness of 458 ± 57 nm which is lower compared to the thin film oxidized on sapphire substrates. Similar to the coating on sapphire substrates the HAADF image (Fig. 8a) suggests the formation of the dark appearing Si rich precipitates in the substrate near region. The oxide scale and remaining coating from Fig. 8 can also be seen in the FIB cut in Fig. 9c. In general, in Fig. 9 all coatings deposited on SiC substrates are compared after 3 and 30 h oxidation at 1200 °C, respectively. For $Hf_{0.21}Si_{0.18}B_{0.61}$ the formation of m-HfO_2 during heating up is strongly visible as bright globular grains in the dark appearing silica oxide scale (Fig. 9a,b). After 30 h oxidation a large amount of additional HfO_2 is formed for $Hf_{0.21}Si_{0.18}B_{0.61}$ – similar to the coating oxidized on sapphire substrate – with only a small amount of remaining HfB_2, as suggested by the XRD analysis of the different oxidized thin films on SiC substrates presented in Fig. 10. Hence, the strong HfO_2 formation after 30 h is independent of the used substrate. One possible explanation for this behavior, could be that the necessary amount of Si, diffusing to the coating/scale interface, can not be maintained over long time periods and hence after a certain time oxidation follows reaction (2) due to the limited kinetics of Eq. (3). Furthermore, no separate Si phase was observed after oxidation for these coatings and therefore Si has a higher tendency to remain within the HfB_2 lattice. These Si atoms however are not able to diffuse to the surface as easy as Si atoms present in precipitates, which can use the column boundaries as fast track diffusion pathways. This result suggests that a certain Si content is necessary to form crystalline Si precipitates and in consequence to enable long term stability in oxidative environment.

For $Hf_{0.20}Si_{0.23}B_{0.57}$ the crystalline Si layer formed after 3 h oxidation time can be clearly seen also in the XRD pattern in Fig. 10c. After 30 h, the Si is consumed and fully oxidized and the crystalline high temperature modification of SiO_2 forms – cristobalite (compare the XRD pattern in Fig. 10c and d). The double peak visible in the XRD pattern at 2 theta ~ 22° suggests both cristobalite structures, tetragonal (SG 92) and cubic (SG 227), respectively. However, to keep the pattern uncluttered just the tetragonal reference lines are shown. For even higher Si contents ($Hf_{0.20}Si_{0.25}B_{0.55}$) some Si is still left after 30 h and a larger amount of cristobalite-SiO_2 forms (see Fig. 10f). Again, similar to the thin films on sapphire substrate recrystallization takes place forming also voids within the remaining coating. Furthermore, the oxide scale thickness of $Hf_{0.20}Si_{0.23}B_{0.57}$ after 30 h is only 750 nm, being half of the thickness measured after oxidation on sapphire substrates, and further underlines the different growth speeds of the oxide grown from the

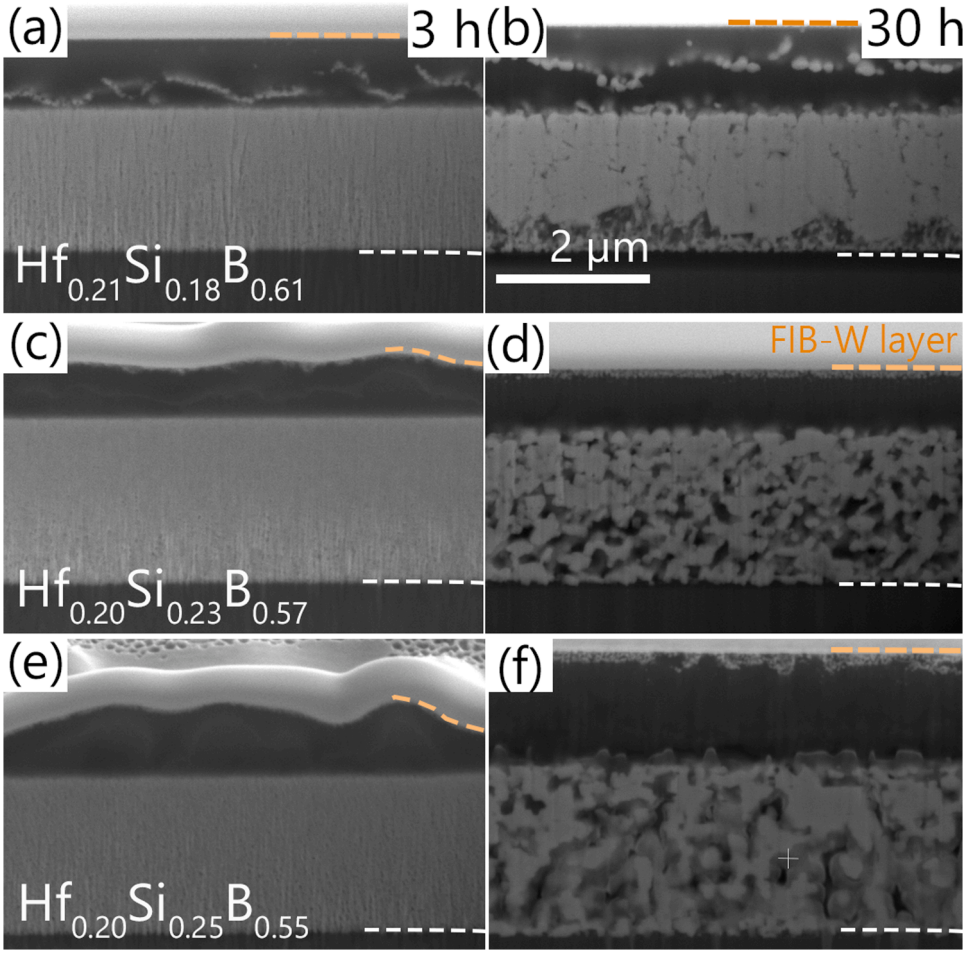

Fig. 9. Isothermal oxidation at 1200 °C of Hf-Si-$B_{2\pm z}$ thin films deposited on single crystalline SiC substrates. FIB cross sections of $Hf_{0.21}Si_{0.18}B_{0.61}$ (a,b), $Hf_{0.20}Si_{0.23}B_{0.57}$ (c,d) and $Hf_{0.20}Si_{0.25}B_{0.55}$ (e,f) are depicted. Dashed white and orange lines indicate the substrate/coating and oxide scale/FIB-tungsten layer interface respectively.

remaining Hf-Si-$B_{2\pm z}$ thin film or the pure Si layers formed at the scale/coating interface. Here, we would like to mention, that in the as deposited state (see Appendix A1) a clear strong peak for the single crystalline SiC substrate is visible at 2 theta = 35.67° (004-orientation) disappearing after oxidation. This suggests that during annealing diffusion processes take place breaking up the high symmetry of the single crystalline substrate in the interface region.

Further oxidation treatments of the $Hf_{0.20}Si_{0.23}B_{0.57}$ thin film grown on SiC substrate at 1300, 1400, and 1500 °C (for 3, 2, and 1 h, respectively) reveals a similar scale formation process (see Fig. 11). The remaining recrystallized thin film (bright appearing) is covered by an amorphous oxide scale (dark appearing). Additional XRD measurements after each treatment (shown in the Appendix, Fig. A2) highlight, that only minor amounts of HfO_2 (less intense peaks) are formed as along with the pure Si phase. However, no signs of a crystalline SiO_2 can be indicated, suggesting a time depended formation of the cristobalite phase. Overall, at these higher temperatures, of course, the scale growth is accelerated and the recrystallization of the remaining coating is much faster progressing.

4. Conclusion

Within this study, we demonstrate the long-term oxidation resistance of physical vapor deposited Hf-Si-$B_{2\pm z}$ thin films revealing low oxide scale growth rates at 1200 °C and even further. To gain a broad insight on the scale formation processes of Hf-Si-$B_{2\pm z}$ coatings, the composition was varied between $Hf_{0.21}Si_{0.18}B_{0.61}$, $Hf_{0.20}Si_{0.23}B_{0.57}$, and $Hf_{0.20}Si_{0.25}B_{0.55}$, respectively. Increasing Si contents lead to smaller column diameters in the as deposited state, accompanied by a non-homogeneous distribution of Si within the Hf-Si-$B_{2\pm z}$ coating morphology (proven by 3D atom probe tomography). At 1200 °C the decomposition process of metastable Hf-Si-$B_{2\pm z}$ directs towards two different mechanisms dominated by Si diffusion. On the one hand, Si is heading towards the surface forming protective silicon rich oxide scales, whereas above 23 at% additional Si-rich zones are formed. Next to Si precipitates within the thin film morphology, pure Si layers on top (remaining coating/scale interface) and bottom (remaining coating/substrate interface) of the Hf-Si-$B_{2\pm z}$ thin films are formed during oxidation. This strong Si diffusion and decomposition is the foundation for the required kinetics being necessary to favor the thermodynamically preferred oxidation of Si. This results in a highly protective oxide scale, which is mainly composed of silicon and oxygen, but containing no HfO_2 even after 60 h at 1200 °C. Furthermore, the scale growth rate of 1.56 µm at 1200 °C for 60 h is clearly below alumina scale formers (e.g. 5–7 µm after 60 h at 1200 °C [38,39]). The consumption of the formed Si precipitates during oxidation results in voids within the unoxidized coating, which however does not impair the coating adhesion for long time periods (tested up to 60 h at 1200 °C) as well as higher temperatures (up to 1500 °C on SiC). Oxidation tests of Hf-Si-$B_{2\pm z}$ coated SiC substrates depict a similar scale formation mechanism, with a more distinct Si diffusion profile towards the remaining coating/oxide scale interface. Hence, this study showcases the high potential of Hf-Si-$B_{2\pm z}$ thin films as oxidation protective coating material, highlighting the various facets of Si dominated scale formation.

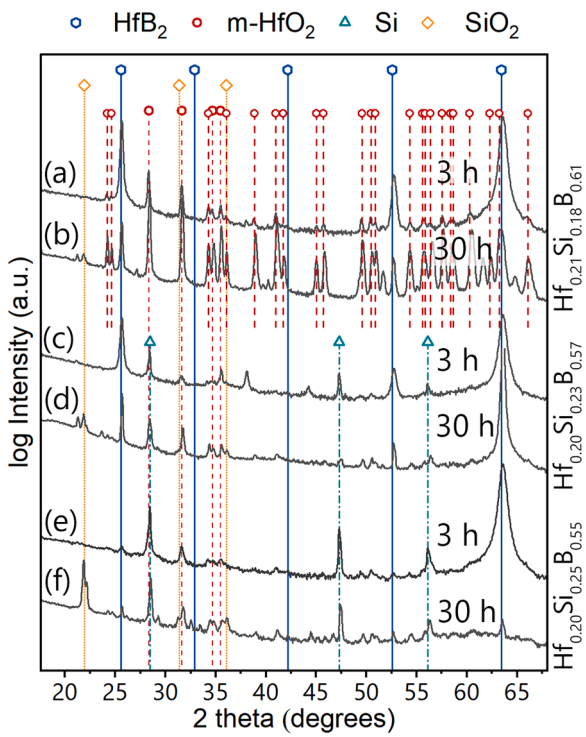

Fig. 10. XRD analysis of Hf-Si-$B_{2\pm z}$ thin films deposited on single crystalline SiC substrates after isothermal oxidation at 1200 °C. Spectra (a-f) correspond to the same coatings as for the FIB cuts (a-f) shown in Fig. 9. Reference patterns are taken from Ref. [47–50].

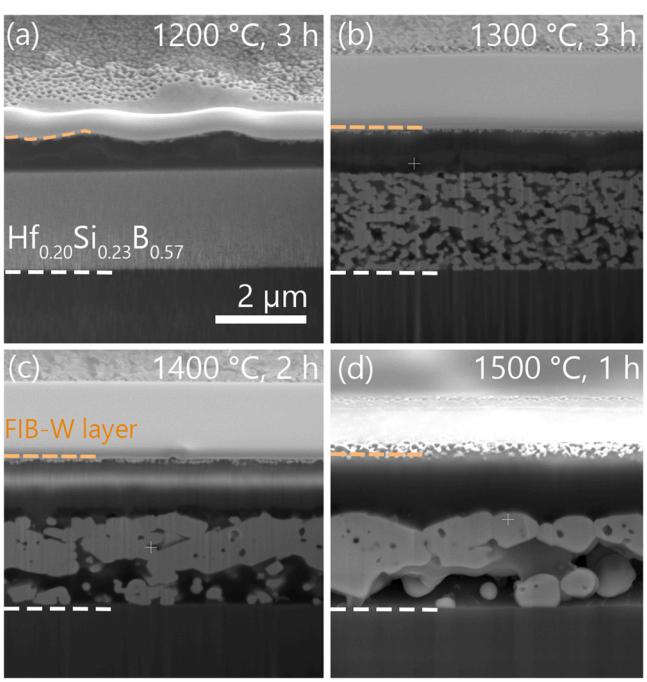

Fig. 11. Oxidation of $Hf_{0.20}Si_{0.23}B_{0.57}$ on SiC substrate at increasing temperatures, 1200–1500 °C. FIB cuts of the oxidized coatings with the substrate/coating interface indicated by a white dashed line and the interface between oxide scale and FIB-tungsten layer by orange dashed lines (a-d).

CRediT authorship contribution statement

T. Glechner: Conceptualization, Investigation, Writing – original draft. **A. Bahr:** Investigation, Writing – review & editing. **R. Hahn:** Investigation. **T. Wojcik:** Investigation. **M. Heller:** Investigation. **A. Kirnbauer:** Investigation. **J. Ramm:** Resources, Writing – review & editing. **S. Kolozsvari:** Resources. **P. Felfer:** Investigation. **H. Riedl:** Supervision, Writing – review & editing.

Declaration of Competing Interest

The authors declare that they have no known competing financial interests or personal relationships that could have appeared to influence the work reported in this paper.

Data Availability

The data that support the findings of this study are available from the corresponding author upon reasonable request.

Acknowledgments

The financial support by the Austrian Federal Ministry for Digital and Economic Affairs, the National Foundation for Research, Technology and Development and the Christian Doppler Research Association is gratefully acknowledged (Christian Doppler Laboratory "Surface Engineering of high-performance Components"). We also thank for the financial support of Plansee SE, Plansee Composite Materials GmbH, and Oerlikon Balzers, Oerlikon Surface Solutions AG. In addition, we want to thank the X-ray center (XRC) of TU Wien for beam time as well as the electron microscopy center - USTEM TU Wien - for using the SEM and TEM facilities. The authors acknowledge TU Wien Bibliothek for financial support through its Open Access Funding Programme. Support by CRC/SFB 1452 CLINT and the ERC Starting Grant HydMet is gratefully acknowledged.

Appendix A. Supplementary material

Supplementary data associated with this article can be found in the online version at doi:10.1016/j.corsci.2022.110413.

References

[1] J.H. Perepezko, The hotter the engine, the better, Science 326 (2009) 1068–1069.
[2] W. Brandl, H.J. Grabke, D. Toma, J. Krüger, The oxidation behaviour of sprayed MCrAlY coatings, Surf. Coat. Technol. 86–87 (1996) 41–47.
[3] J. Ast, M. Döbeli, A. Dommann, M. Gindrat, X. Maeder, A. Neels, P. Polcik, M. N. Polyakov, H. Rudigier, K.D. von Allmen, B. Widrig, J. Ramm, Synthesis and characterization of superalloy coatings by cathodic arc evaporation, Surf. Coat. Technol. 327 (2017) 139–145.
[4] T. Sadowski, P. Golewski, Loadings in Thermal Barrier Coatings of Jet Engine Turbine Blades: An Experimental Research and Numerical Modeling, Springer, Singapore, 2016.
[5] N.P. Bansal, J. Lamon, Ceramic Matrix Composites: Materials, Modeling And Technology, The American Ceramic Society: Wiley, Hoboken, New Jersey, 2015.
[6] T. Glechner, H.G. Oemer, T. Wojcik, M. Weiss, A. Limbeck, J. Ramm, P. Polcik, H. Riedl, Influence of Si on the oxidation behavior of TM-Si-B2±z coatings (TM = Ti, Cr, Hf, Ta, W), Surf. Coat. Technol. (2022), 128178.
[7] C. Fuger, R. Hahn, L. Zauner, T. Wojcik, M. Weiss, A. Limbeck, O. Hunold, P. Polcik, H. Riedl, Anisotropic super-hardness of hexagonal WB2±z thin films, Mater. Res. Lett. 10 (2022) 70–77.
[8] M.M. Opeka, I.G. Talmy, E.J. Wuchina, J.A. Zaykoski, S.J. Causey, Mechanical, thermal, and oxidation properties of refractory hafnium and zirconium compounds, J. Eur. Ceram. Soc. 19 (1999) 2405–2414.
[9] W.G. Fahrenholtz, G.E. Hilmas, Ultra-high temperature ceramics: materials for extreme environments, Scr. Mater. 129 (2017) 94–99.
[10] L. Silvestroni, G. Meriggi, D. Sciti, Oxidation behavior of ZrB2 composites doped with various transition metal silicides, Corros. Sci. 83 (2014) 281–291.
[11] F.V. Kiryukhantsev-Korneev, M.V. Lemesheva, N.V. Shvyndina, E.A. Levashov, A. Y. Potanin, Structure, mechanical properties, and oxidation resistance of ZrB2, ZrSiB, and ZrSiB/SiBC coatings, Prot. Met. Phys. Chem. Surf. 54 (2018) 1147–1156.
[12] P. Kiryukhantsev-Korneev, A. Sytchenko, Y. Pogozhev, S. Vorotilo, A. Orekhov, P. Loginov, E. Levashov, Structure and properties of Zr-Mo-Si-B-(N) hard coatings obtained by d.c. magnetron sputtering of ZrB2-MoSi2 target, Materials 14 (2021), https://doi.org/10.3390/ma14081932.

[13] X. Ren, H. Li, Y. Chu, Q. Fu, K. Li, Ultra-high-temperature ceramic HfB2-SiC coating for oxidation protection of SiC-coated carbon/carbon composites, Int. J. Appl. Ceram. Technol. 12 (2015) 560–567.
[14] P. Wang, H. Li, R. Yuan, J. Kong, T. Li, Y. Zhang, A. CrSi2-HfB2-SiC, coating providing oxidation and ablation protection over 1973 K for SiC coated C/C composites, Corros. Sci. 167 (2020), 108536.
[15] M. Zhang, X. Ren, H. Chu, J. Lv, W. Li, W. Wang, Q. Yang, P. Feng, Oxidation inhibition behaviors of the HfB2-SiC-TaSi2 coating for carbon structural materials at 1700° C, Corros. Sci. 177 (2020), 108982.
[16] W.G. Fahrenholtz, G.E. Hilmas, Oxidation of ultra-high temperature transition metal diboride ceramics, Int. Mater. Rev. 57 (2012) 61–72.
[17] X. Cai, S. Ding, K. Wen, L. Xu, H. Xue, S. Xin, T. Shen, Unmasking the anomalous rapid oxidation of refractory TiB2 at low temperatures, J. Eur. Ceram. Soc. 41 (2021) 5100–5108.
[18] W.G. Fahrenholtz, G.E. Hilmas, I.G. Talmy, J.A. Zaykoski, Refractory diborides of zirconium and hafnium, J. Am. Ceram. Soc. 90 (2007) 1347–1364.
[19] T. Glechner, O.E. Hudak, T. Wojcik, L. Haager, F. Bohrn, H. Hutter, O. Hunold, J. Ramm, S. Kolozsvári, E. Pitthan, D. Primetzhofer, H. Riedl, Influence of the non-metal species on the oxidation kinetics of Hf, HfN, HfC, and HfB2 coatings, Mater. Des. 211 (2021), 110136.
[20] C. Fuger, B. Schwartz, T. Wojcik, V. Moraes, M. Weiss, A. Limbeck, C.A. Macauley, O. Hunold, P. Polcik, D. Primetzhofer, P. Felfer, P.H. Mayrhofer, H. Riedl, Influence of Ta on the oxidation resistance of WB2−z coatings, J. Alloy. Compd. 864 (2021), 158121.
[21] J. Thörnberg, B. Bakhit, J. Palisaitis, N. Hellgren, L. Hultman, G. Greczynski, P.O. Å. Persson, I. Petrov, J. Rosen, Improved oxidation properties from a reduced B content in sputter-deposited TiBx thin films, Surf. Coat. Technol. 420 (2021), 127353.
[22] B. Bakhit, S. Dorri, A. Kooijman, Z. Wu, J. Lu, J. Rosen, J.M.C. Mol, L. Hultman, I. Petrov, J.E. Greene, G. Greczynski, Multifunctional ZrB2-rich Zr1-xCrxBy thin films with enhanced mechanical, oxidation, and corrosion properties, Vacuum 185 (2021), 109990.
[23] M.M. Opeka, I.G. Talmy, J.A. Zaykoski, Oxidation-based materials selection for 2000°C + hypersonic aerosurfaces: theoretical considerations and historical experience, J. Mater. Sci. 39 (2004) 5887–5904.
[24] B. Grančič, M. Mikula, T. Roch, P. Zeman, L. Satrapinskyy, M. Gregor, T. Plecenik, E. Dobročka, Z. Hájovská, M. Mičušík, A. Šatka, M. Zahoran, A. Plecenik, P. Kúš, Effect of Si addition on mechanical properties and high temperature oxidation resistance of Ti–B–Si hard coatings, Surf. Coat. Technol. 240 (2014) 48–54.
[25] E. Aschauer, T. Wojcik, P. Polcik, O. Hunold, M. Arndt, V. Dalbauer, P. H. Mayrhofer, P. Felfer, H. Riedl, Ultra-high oxidation resistance of nano-structured thin films, Mater. Des. 201 (2021), 109499.
[26] E. Rudy, Ternary Phase Equilibria in Transition Metal-boron-carbon-silicon Systems. Part 5. Compendium of Phase Diagram Data, 1969. ⟨https://apps.dtic.mil/sti/pdfs/AD0689843.pdf⟩, (Accessed 16 July 2021).
[27] T. Glechner, R. Hahn, L. Zauner, S. Rißlegger, A. Kirnbauer, P. Polcik, H. Riedl, Structure and mechanical properties of reactive and non-reactive sputter deposited WC based coatings, J. Alloy. Compd. 885 (2021), 161129.
[28] D.A. Shirley, High-resolution X-ray photoemission spectrum of the valence bands of gold, Phys. Rev. B Condens. Matter 5 (1972) 4709–4714.
[29] J.H. Scofield, Hartree-Slater subshell photoionization cross-sections at 1254 and 1487 eV, J. Electron Spectrosc. Relat. Phenom. 8 (1976) 129–137.
[30] P. Felfer, Atom-Probe-Toolbox: Matlab Toolbox for APT analysis, Github, n.d. ⟨https://github.com/peterfelfer/Atom-Probe-Toolbox⟩, (Accessed 11 October 2021).
[31] I. Petrov, P.B. Barna, L. Hultman, J.E. Greene, Microstructural evolution during film growth, J. Vac. Sci. Technol. A. 21 (2003) S117–S128.
[32] S. Vepřek, S. Reiprich, L. Shizhi, Superhard nanocrystalline composite materials: the TiN/Si3N4 system, Appl. Phys. Lett. 66 (1995) 2640–2642.
[33] G. Mavel, J. Escard, P. Costa, J. Castaing, ESCA surface study of metal borides, Surf. Sci. 35 (1973) 109–116.
[34] H.T. Johnson-Steigelman, A.V. Brinck, S.S. Parihar, P.F. Lyman, Hafnium silicide formation on $\text{Si}(001)$, Phys. Rev. B Condens. Matter. 69 (2004), 235322.
[35] L. Chen, T. Goto, T. Hirai, T. Amano, State of boron in chemical vapour-deposited SiC-B composite powders, J. Mater. Sci. Lett. 9 (1990) 997–999.
[36] L. Hultman, J. Bareño, A. Flink, H. Söderberg, K. Larsson, V. Petrova, M. Odén, J. E. Greene, I. Petrov, Interface structure in superhard TiN-SiN nanolaminates and nanocomposites: film growth experiments and ab initio calculations, Phys. Rev. B Condens. Matter. 75 (2007), 155437.
[37] D.J. Tallman, B. Anasori, M.W. Barsoum, A critical review of the oxidation of Ti2AlC, Ti3AlC2 and Cr2AlC in air, Mater. Res. Lett. 1 (2013) 115–125.
[38] S. Kota, E. Zapata-Solvas, Y. Chen, M. Radovic, W.E. Lee, M.W. Barsoum, Isothermal and Cyclic Oxidation of MoAlB in Air from 1100°C to 1400°C, J. Electrochem. Soc. 164 (2017) C930.
[39] G.M. Song, V. Schnabel, C. Kwakernaak, S. van der Zwaag, J.M. Schneider, W. G. Sloof, High temperature oxidation behaviour of Ti2AlC ceramic at 1200°C, Mater. High Temp. 29 (2012) 205–209.
[40] J.-O. Achenbach, R. Sahu, B. Völker, M. Hans, D. Primetzhofer, D.J. Miljanovic, C. Scheu, J.M. Schneider, Synthesis and properties of orthorhombic MoAlB coatings, Coat. World 9 (2019) 510.
[41] B.E. Deal, A.S. Grove, General relationship for the thermal oxidation of silicon, J. Appl. Phys. 36 (1965) 3770–3778.
[42] R. Hollerweger, H. Riedl, J. Paulitsch, M. Arndt, R. Rachbauer, P. Polcik, S. Primig, P.H. Mayrhofer, Origin of high temperature oxidation resistance of Ti–Al–Ta–N coatings, Surf. Coat. Technol. 257 (2014) 78–86.
[43] Y. Moritz, C. Saringer, M. Tkadletz, A. Stark, N. Schell, I. Letofsky-Papst, C. Czettl, M. Pohler, N. Schalk, Oxidation behavior of arc evaporated TiSiN coatings investigated by in-situ synchrotron X-ray diffraction and HR-STEM, Surf. Coat. Technol. 404 (2020), 126632.
[44] W.G. Fahrenholtz, Thermodynamic analysis of ZrB2?SiC oxidation: formation of a SiC-depleted region, J. Am. Ceram. Soc. 90 (2007) 143–148.
[45] M. Klinger, More features, more tools, more CrysTBox, J. Appl. Crystallogr. 50 (2017) 1226–1234.
[46] M. Klinger, A. Jäger, Crystallographic tool box (CrysTBox): automated tools for transmission electron microscopists and crystallographers, J. Appl. Crystallogr. 48 (2015) 2012–2018.
[47] International Center of Diffraction Data, Powder diffraction file 04-002-0174, 2019.
[48] International Center of Diffraction Data, Powder diffraction file 04-004-3850, 2019.
[49] International Center of Diffraction Data, Powder diffraction file 04-006-4528, 2019.
[50] International Center of Diffraction Data, Powder diffraction file 04-005-4875, 2019.